

Study on the Regulated Cell Death of Hypertrophic H9c2 Cells Induced by Au:Ag Nanoparticles

Andrés G Galindo-Padrón ^{1,*}, Helen Yarimet Lorenzo-Anota ^{2,3,*}, Mayte Rueda-Munguía^{2,3}, Alejandra García-Carrasco ¹, Mabel Gaitán López ¹, Eduardo Vázquez-Garza², Enrique Campos-González⁴, Omar Lozano ^{2,3,5}, Jorge L Cholula-Díaz ¹

¹School of Engineering and Sciences, Tecnológico de Monterrey, Monterrey, Nuevo Leon, Mexico; ²Institute for Obesity Research, Tecnológico de Monterrey, Monterrey, Nuevo Leon, Mexico; ³School of Medicine and Health Sciences, Tecnológico de Monterrey, Monterrey, Nuevo Leon, Mexico; ⁴Departamento de Física, Instituto Nacional de Investigaciones Nucleares, Ocoyoacac, Mexico; ⁵Cátedra de Cardiología y Medicina Vasculat, Tecnológico de Monterrey, Monterrey, Nuevo León, México

*These authors contributed equally to this work

Correspondence: Omar Lozano; Jorge L Cholula-Díaz, Email omar.lozano@tec.mx; jorgeluis.cholula@tec.mx

Background and Aim: Over the past years, noble metal-based nanoparticles have been extensively investigated for their applications in nanomedicine. However, there are still concerns about the potential adversities that these nanoparticles may present in an organism. In particular, whether they could cause an exacerbated cytotoxic response in susceptible tissues due to damage or disease, such as the heart, liver, spleen, or kidneys. In this regard, this study aims to evaluate the cytotoxicity of mono- and bimetallic nanoparticles of gold and silver (Au:Ag NPs) on healthy and hypertrophic cardiac H9c2 cells, and on healthy and metabolically activated macrophages derived from U937 cells. The main objective of this work is to explore the susceptibility of cells due to exposure to Au:Ag NPs in conditions representing cardiometabolic diseases.

Methods: Au:Ag NPs were synthesized in different molar ratios (Au:Ag, 100:0, 75:25, 50:50, 25:75, 0:100) using starch as a capping and reducing agent. Their physicochemical properties were characterized through UV-vis spectroscopy, X-ray diffraction (XRD), Fourier transform infrared (FTIR) spectroscopy, dynamic light scattering (DLS), ζ -potential measurements, and transmission electron microscopy (TEM). Moreover, the effect of the metal-based nanoparticle exposure on healthy and hypertrophic H9c2 cells was measured by analyzing the cellular vitality, the loss of mitochondrial membrane potential ($\Delta\Psi_m$), and the production of mitochondrial reactive oxygen species (mROS).

Results: The Au:Ag NPs did not affect the cell vitality of healthy or metabolically activated macrophages. On the contrary, healthy H9c2 cells showed decreased mitochondrial metabolism when exposed to NPs with higher Ag concentrations. Furthermore, hypertrophic H9c2 cells were more susceptible to the same NPs compared to their non-hypertrophic counterparts, and presented a pronounced loss of $\Delta\Psi_m$. In addition, these NPs increased the production of mROS and regulated cell death in both cardiac cells.

Conclusion: In conclusion, low doses of high-Ag load in Au:Ag NPs produced cytotoxicity on H9c2 cardiac cells, with hypertrophic cells being more susceptible. These results suggest that cardiac hypertrophic conditions are more prone to a cytotoxic response in the presence of bimetallic Au:Ag NPs compared to healthy cells. In addition, this work opens the door to explore the nanotoxicity of noble metal-based NPs in biological disease conditions.

Keywords: cardiovascular disease, hypertrophic cardiomyoblasts, bimetallic nanoparticles, metabolically activated macrophages

Introduction

Cardiometabolic disease is a cluster of interrelated conditions that increase the risk of cardiovascular diseases (CVDs), coronary artery disease and metabolic disorders.¹ These conditions often overlap and include insulin resistance, hypertension, dyslipidemia, systemic inflammation, and obesity.²⁻⁴ In this regard, obesity is linked to the progression

of several CVDs, the primary cause of death worldwide, being the cause of death of approximately 20.5 million people in 2021 alone,^{5,6} including hypertrophic cardiomyopathy.⁷ Hypertrophy is an adaptive response to CVDs, which involves an increase in muscle mass. When this occurs in the cardiac system, it causes the cardiomyocytes to enlarge, allowing the heart to reduce wall tension.^{8,9} Furthermore, CVDs are frequently linked to metabolic disorders that undermine the immune system through persistent chronic inflammation.¹⁰ This chronic inflammatory state leads to an increase in the number of metabolically activated (MA) macrophages, which in turn aggravate metabolic disorders and their presence is highly correlated with CVDs such as coronary heart disease.^{11–13} MA macrophages play a crucial role in the pathophysiology of these conditions by perpetuating inflammation and contributing to tissue remodeling and fibrosis. Macrophages, especially those in a metabolically activated state, result critically in the progression of obesity and CVDs due to their involvement in lipid metabolism, and interaction with other cell types within the immune system. It is believed that, unlike healthy cells, cells with alterations such as hypertrophic cells could be more susceptible when exposed to nanomaterials due to their altered cellular metabolism.^{14,15}

In recent years, nanomaterials have been employed in medical applications for imaging purposes, due to their unique characteristics such as high mobility throughout the body, large surface area-to-volume ratio, and imaging versatility.^{8,9,16} Particularly, metallic nanomaterials have been employed in the diagnosis of CVDs,¹⁷ and more recently, have been extensively investigated for therapeutic purposes.^{18,19} In this regard, metallic nanoparticles (NPs) have gained significant interest in the medical field for pharmaceutical applications, due to their unique optical and electrical properties, as well as their excellent biocompatibility.²⁰ However, it has been reported that the exposure to some of these NPs may cause a breakdown of the cellular buffering system by interfering with cellular mechanisms, such as by impairing mitochondrial function.²¹ Particularly, silver (Ag) NPs have shown to decrease the mitochondrial membrane potential ($\Delta\Psi_m$), which leads to a decrease in ATP production as well as an increase in mitochondrial superoxide generation on diverse cells, including those of cancerous and cardiac nature.^{22,23}

Among the various types of metallic NPs, Ag and gold (Au) NPs stand out, due to their antibacterial and biocompatibility properties, respectively.^{24–27} Historically, Au NPs have been used for cancer-related applications in the cardiovascular area, taking advantage of their bioactivity.²⁸ Au NPs also have exhibited inherent antioxidant properties, such as catalase-mimic and peroxidase-like activities that may be useful for CVDs control.^{20,29} However, to the best of our knowledge, the cytotoxicity of Au and Ag NPs under pathological conditions such as cardiometabolic disease has not been described yet. Furthermore, Ag NPs are an attractive approach to destroy bacterial drug resistance as they present inhibitory and anti-microbial activity.^{30,31} Bimetallic Au and Ag NPs (Au:Ag NPs) have opened a new field of research due to their broad-spectrum of capabilities in the biomedical field, such as antibacterial and wound healing, owing to the synergy between the metals that make up their composition.³² Au:Ag NPs exhibit electronic, optical, and catalytic properties that surpass monometallic nanostructures, making the use of Au attractive to modulate Ag toxicity, such as in cardiometabolic diseases.²⁴

Hence, to associate possible applications of noble metal-based NPs in metabolic disorders, it is first important to explore their nanotoxicology under pathological conditions. In this regard, here we investigated the cytotoxicity and cell death mechanism induction of mono- and bimetallic Au:Ag NPs on *in vitro* cellular models that are related to metabolic disorders, ie, hypertrophic cardiac cells, and metabolically activated macrophages. We also compared the NP cytotoxic susceptibility of these models with their healthy counterpart.

Materials and Methods

Reagents and Materials

Sodium tetrachloroaurate (NaAuCl_4) and sodium bicarbonate (NaHCO_3) were purchased from Sigma Aldrich (St. Louis, MO, USA). Silver nitrate (AgNO_3 99%) and nitric acid (HNO_3 70%) were purchased from Fermont (Monterrey, N.L., Mexico). Starch, sodium hydroxide (NaOH), sodium carbonate (Na_2CO_3) and potassium sodium tartrate ($\text{KNaC}_4\text{H}_4\text{O}_6$) were purchased from CTR Scientific (Monterrey, N.L., Mexico). All chemicals were used without any purification step, Au:Ag NPs synthesis and characterization were carried out using deionized (DI) water, while biological experiments were conducted using double distilled water.

Prior to their use, all glassware and magnetic stirring bars used were kept in a 1:8 hydrochloric acid (HCl, Sigma Aldrich, ST. Louis, MO, USA) solution for 24 h, then they were transferred to a 1 M NaOH solution for 24 h and were thoroughly rinsed with DI water. Both solutions were made with DI water.

Au:Ag Nanoparticle Synthesis

The synthesis of colloidal monometallic (Au NPs and Ag NPs) and bimetallic Au:Ag NPs was carried out using a modified version of previously reported synthesis methods.^{33,34} First, a 1% w/v starch solution was added to 9.5 mL of DI water at $70 \pm 1^\circ\text{C}$ with an adjusted pH of 11. Afterwards, the corresponding metal precursor solution ratio was added using the amounts shown in Table 1. The reaction occurred under constant stirring for 2 h in a water bath at a reaction temperature of $70 \pm 1^\circ\text{C}$. The resulting colloidal NPs were washed by centrifugation and re-dispersed for further characterization and biomedical tests.

UV-Visible Spectroscopy

UV-visible spectra of the colloidal NPs were obtained using a PerkinElmer 365 spectrometer (PerkinElmer Inc, Waltham, Ma, USA). The colloidal samples were diluted in a 1:5 ratio with DI water. The absorption spectra of the samples were measured in the range of 300–800 nm with a scan rate of 300 nm/min and a scan step of 0.5 nm. The absorption spectra of each sample were measured at the same day of synthesis and tracked at 14 and 26 days after synthesis to monitor the colloidal stability.

Powder X-Ray Diffraction Analysis

Powder XRD patterns of the Au:Ag NPs were analyzed with a Rigaku Miniflex 600 diffractometer (Rigaku, Tokyo, Japan) using a 40 kV voltage, a current of 15 mA, and a Cu K α radiation source ($\lambda=1.542 \text{ \AA}$). All patterns were recorded at room temperature using a scan speed of $3^\circ/\text{min}$ and a step width of 0.05° in the range of $25\text{--}80^\circ$ (2θ). The XRD samples were prepared by drying dropwise 3–5 mL of the colloidal suspensions on a glass sample holder at $\sim 100^\circ\text{C}$.

The lattice parameter (a) was calculated using Bragg's law ($\lambda = 2 d_{hkl} \sin\theta_{hkl}$)³⁵ and the relation between d_{hkl} and a , where λ is the radiation wavelength, d_{hkl} corresponds to the interplanar distance for parallel planes with Miller indices (hkl), and θ_{hkl} is the angle of diffraction. The average crystallite size (L) was calculated using the Debye-Scherrer equation ($L=k \lambda/[B\cos\theta_{hkl}]$),³⁴ where L is the nanoparticle's crystallite size, k represents the Scherrer constant, assuming $k=0.94$ (for spherical particles), and B is the full width at half maximum (FWHM).

Fourier Transform Infrared (FT-IR) Spectroscopy

FT-IR spectra of the Au:Ag NPs were obtained using a PerkinElmer Spectrum 400 FT-IR/FT-NIR (Perkin-Elmer, Waltham, MA, USA) in attenuated total reflectance (ATR) mode. The spectra were measured between 600 and 4000 cm^{-1} .

Table 1 Experimental Conditions for the Synthesis of Colloidal Au, Ag, and Au:Ag NPs. In All Cases, 500 μL of a 1% w/v Starch Solution Was Used

| NPs (Au:Ag) | 25 mm NaAuCl ₄ (μL) | 25 mm AgNO ₃ (μL) |
|-------------|---|---|
| Au | 250 | 0 |
| Au75:Ag25 | 187 | 63 |
| Au50:Ag50 | 125 | 125 |
| Au25:Ag75 | 63 | 187 |
| Ag | 0 | 250 |

Abbreviations: NPs, Nanoparticles; Au:Ag, Gold:Silver; NaAuCl₄, Sodium tetrachloroaurate; AgNO₃, Silver nitrate.

Dynamic Light Scattering (DLS)

Hydrodynamic diameter (D_H) and particle size distribution (PSD) analysis by dynamic light scattering (DLS) were carried out using a Malvern Zetasizer Nano ZS (Malvern Instruments, Malvern, UK). Measurements were carried out without diluting the colloidal NP samples, at $25 \pm 0.1^\circ\text{C}$, using 1 mL disposable ζ -potential cells (Malvern, DTS 1070), and a He-Ne laser ($\lambda = 633 \text{ nm}$) with a backscattering detection configuration (173°). The Au NP sample measurements were done using a refractive index of 0.700 and an absorption of 3.320, while the Ag NP sample was measured using a refractive index of 0.135 and an absorption of 3.390. All the bimetallic nanoparticles (Au75:Ag25, Au50:Ag50 and Au25:Ag75) samples were measured using a refractive index of 0.200 and an absorption value of 3.320.

Electrophoretic Light Scattering (ELS)

Electrophoretic light scattering (ELS) was used to measure the ζ -potential of the NPs. Measurements for the determination of colloidal stability were carried out using a Malvern Zetasizer Nano ZS (Malvern Instruments, Malvern, UK). Measurements were carried out without diluting the colloidal NP samples, at $25 \pm 0.1^\circ\text{C}$, using 1 mL disposable ζ -potential cells (Malvern, DTS 1070) and a He-Ne laser ($\lambda = 633 \text{ nm}$) with a backscattering detection configuration (173°).

Transmission Electron Microscopy (TEM)

The size and shape of the bimetallic Au:Ag NPs were analyzed by transmission electron microscopy (TEM) with a JEOL JEM-2010 equipment, operated with an acceleration voltage of 200 kV. The specimen was prepared by placing a drop of the colloid directly on a formvar-coated copper grid and allowing the dispersion medium to evaporate at room temperature. The TEM images were processed by ImageJ software to obtain the size distributions of nanoparticles.

H9c2 Cell Culture

Neonatal rat ventricular myoblast H9c2 cell line (ATCC, CRL-1446) was purchased from ATCC. Cells were cultured in Dulbecco's modified Eagle medium (DMEM) (Sigma Aldrich, ST. Louis, MO, USA) supplemented with 10% fetal bovine serum (FBS, Biowest, Riverside, MO, USA), and penicillin-streptomycin (Gibco[®] by Life Technologies, Carlsbad, CA, USA) which contained 100 U/mL penicillin and 100 $\mu\text{g}/\text{mL}$ streptomycin. The cell cultures were incubated in a Sanyo MCO-18AIC (UV) CO₂ Incubator at 37°C in an air-humidified 5% CO₂ atmosphere. Cell detachment was performed using 0.25% trypsin-EDTA (Gibco[®] by Life Technologies, Carlsbad, CA, USA) and cell quantification using a trypan blue solution (Sigma Aldrich, St. Louis, MO, USA) in a Neubauer-improved counting chamber.

H9c2 Hypertrophy Induction

The H9c2 cells were cultured as previously described, cells were seeded at 4×10^3 per well in 24-well plates. Cells were deprived to 1% FBS supplemented DMEM for 24 h, afterwards, they received two stimuli of angiotensin II ($1\mu\text{g}/\mu\text{L}$; TOCRIS, Bristol, UK) each 24 h during two consecutive days.

U937 Differentiation Into Macrophages

Macrophages were derived from the U937 human lymphoblast monocytes cell line (ATCC, CRL-1593). They were cultured in RPMI-1640 medium, supplemented with 10% FBS (Biowest, Riverside, MO, USA), and penicillin-streptomycin (Gibco[®] by Life Technologies, Carlsbad, CA, USA) which contained 100 U/mL penicillin and 100 $\mu\text{g}/\text{mL}$ streptomycin. The cell cultures were incubated in a Sanyo MCO-18AIC (UV) CO₂ incubator at 37°C in an air-humidified 5% CO₂ atmosphere. In order to induce differentiation of U937 monocyte cells to the macrophage phenotype, 2×10^5 cells were incubated with culture media supplemented with 50 ng/mL phorbol 12-myristate 13-acetate (PMA, Sigma Aldrich, ST. Louis, MO, USA) for 72 h. Subsequently, the cells were washed twice with 100 μL of sterile phosphate buffer solution (PBS, Sigma Aldrich, ST. Louis, MO, USA) and incubated for an additional 24 h in RPMI-1640 without PMA.

Macrophages Induction for Metabolic Activation

Macrophages were differentiated from U937 cells, as described in the previous section. Afterwards, to induce a metabolically activated macrophage state, they were treated with Bovine Serum Albumin (BSA) (Sigma Aldrich, ST. Louis, MO, USA) conjugated with palmitic acid (PA) (Sigma Aldrich, ST. Louis, MO, USA) at a 1:6 molar ratio equivalent to 200 μM , for 24 h, and were kept in incubation at 37 °C in an air humidified 5% CO_2 atmosphere.

Protein Quantification

Cells were washed before being detached using trypsin and lysed with Triton X-100 solution. Protein content was determined by Lowry assay. This assay is based on the biuret reaction, where Cu^+ ions react with peptides to form a copper-protein complex, and the subsequent reaction of said copper-protein complex with the Folin-Ciocalteu reagent (Merck, Darmstadt, Germany), resulting in a blue color that is proportional to the protein concentration. Samples were incubated with biuret solution (4 mg/mL NaOH, 20 mg/mL Na_2CO_3 , 10 mg/mL $\text{KNaC}_4\text{H}_4\text{O}_6$, and 5 mg/mL CuSO_4), and finally samples were incubated with Folin solution in a 1:10 (v:v) ratio (Merck, Darmstadt, Germany). Bovine serum albumin (Sigma Aldrich, St. Louis, MO, USA) was used as a standard curve. The quantification was read on the spectrophotometer BioTek Synergy HT (BioTek, Winooski, VT, USA) by fluorescence excitation and emission measured at 530 and 590 nm, respectively.

Cell Vitality Assay

For the in vitro cell vitality assay, H9c2 and hypertrophic H9c2 cells were seeded at 4×10^3 cells/well in 100 μL DMEM media, and were treated with different concentrations (0.1, 0.5, 1, 5 and 10 ppm) of mono- and bimetallic NPs for 24 h. Macrophages were seeded at 2×10^5 cells/well in 200 μL of RPMI media underwent the same concentrations (0.1, 0.5, 1, 5 and 10 ppm) of metallic NPs for 24 h. Afterwards, 5 mg/mL of alamar blue (Thermo Fisher Scientific, Waltham, MA, USA) was added to each cell well, and was incubated for 4 h at 37 °C without exposure to light. Fluorescence excitation and emission were measured at 530 and 590 nm, respectively, using a microplate BioTek Synergy HT (BioTek, Winooski, VT, USA).

The half maximal inhibitory concentration (IC_{50}) was calculated for each type of nanoparticle treatment and for both cell types by analyzing the inhibitor concentration versus the normalized response. The vitality percentage was calculated using the following equation:

$$\text{vitality (\%)} = \frac{\text{sample} - \text{blank}}{\text{control} - \text{blank}} \times 100$$

where sample, control and blank represent the average fluorescence for each NP treatment, non-treated cells and wells with no cells, respectively.

The normalized response described by the Hill-Langmuir equation was fitted to the following equation through a nonlinear regression:

$$f(x) = \text{Min} + \frac{\text{Max} - \text{Min}}{1 + \left(\frac{x}{\text{IC}_{50}}\right)^H}$$

where Max and Min are the maximum and minimum cell vitality, and are set to 100 and 0, respectively, x corresponds to NPs concentration (ppm) and H is the Hill coefficient.

Cell Viability Analysis

Cell viability analysis was analyzed using Ghost dye satin (eBioscience, Waltham, MA, USA). In brief, cells were seeded in 12-well plates (Corning Inc. Costar[®], Corning, NY, USA) and treated with the previously calculated IC_{50} of Ag and Au₂₅:Ag₇₅ NPs for 24 h. Afterwards, cells were collected and incubated with Ghost dye satin (eBioscience, Waltham, MA, USA) for 15 min at 37 °C in darkness. Then, cells were washed with PBS and analyzed using flow cytometry (CytoFLEX, Beckman Coulter, California, USA).

Mitochondrial Membrane Potential Analysis ($\Delta\Psi_m$)

$\Delta\Psi_m$ was measured using JC-1 staining (Thermo Scientific, Waltham, MA, USA). H9c2 cells were seeded in 12-well plates (Corning Inc. Costar[®], Corning, NY, USA) and treated with the previously calculated IC₅₀ for Ag and Au25:Ag75 NPs for 24 h. Afterwards, cells were collected and incubated with the medium containing JC-1 (1 μ M) for 20 min at 37 °C in darkness. Then, cells were washed with PBS and stained with Ghost dye satin (eBioscience, Waltham, MA, USA) for 15 min at 37 °C in darkness. Finally, cells were washed with PBS and analyzed using flow cytometry (CytoFLEX, Beckman Coulter, California, USA), as previously described. The levels of $\Delta\Psi_m$ are represented in percentage of red fluorescence intensity and green fluorescence intensity.

Mitochondrial Reactive Oxygen Species (mROS) Analysis

The mROS production levels were assessed with MitoSOX[™] Red mitochondrial superoxide indicator (Thermo Fisher Scientific, Waltham, MA, USA). Cells at a density of 1×10^5 cells/well were seeded in 24-well plates (Corning Inc. Costar[®], Corning, NY, USA) and treated with the IC₅₀ of Ag and Au25:Ag75 NPs, and 50 μ M H₂O₂ as a positive control, all of them for 24 h. Afterwards, the medium was removed and washed with DMEM before detaching the cells with 0.25% trypsin-EDTA, cells were then centrifuged for 5 min at 500 g. MitoSox[™] Red (200 μ L) was added for 20 min at 37 °C. MitoSox[™] Red was analyzed using 510 nm and 580 nm for excitation and emission wavelengths, respectively, using a BD FACS CANTO II flow cytometer (BD Biosciences, Heidelberg, Germany). Data was analyzed with the FlowJo Software (Tree Star Inc., Ashland, OR, USA).

Cell Death Analysis

H9c2 cell death was determined by analyzing phosphatidylserine (PS) exposure and cell-membrane permeabilization, using Annexin V-allophycocyanin (APC) (AnnV, 0.25 μ g/mL; BD Biosciences Pharmingen, San Jose, CA, USA) and propidium iodide (PI; 0.5 μ g/mL; Milliporesigma, Eugene, OR, USA), respectively. H9c2 and hypertrophic H9c2 cells, at a density of 1×10^5 cells/well, were cultured and treated with the previously calculated IC₅₀ of Ag and Au25:Ag75 NPs for 24 h. After treatment, cells were washed and resuspended in binding buffer (10 mM HEPES/NaOH pH 7.4, 140 mM NaCl, 2.5 mM CaCl₂), and stained with AnnV (0.1 μ g/mL) and PI (0.5 μ g/mL) for 30 min at 4 °C. Cells were analyzed by flow cytometry (FACS CANTO II, BD Biosciences, Heidelberg, Germany). Data was analyzed with the FlowJo Software (Tree Star Inc., Ashland, OR, USA).

Statistical Analysis

The data were analyzed using the software GraphPad Prism (GraphPad Software, San Diego, CA, USA). Results are presented as the mean \pm standard error of the mean (SEM) of at least three independent experiments. Statistical analysis was done using a paired Student's *t*-test. The statistical significance was defined as $p < 0.05$.

Results

Physicochemical Characterization of Mono- and Bimetallic Au:Ag NPs

The eco-friendly synthesis of the colloidal Au:Ag NPs was performed employing starch as the reducing and capping agent for the Ag⁺ and AuCl₄⁻ ions through a wet chemical reduction.^{33,34} In [Supplementary Figure S1](#), a shift in coloration from red (Au NPs) to brown (Ag NPs) depending on the amount of Au and Ag added can be observed, which indicates the synthesis of colloidal Au:Ag NPs with different chemical compositions. To investigate the optical properties of the synthesized NPs, UV-vis spectroscopy was performed as shown in [Figure 1A](#). The obtained optical spectra exhibited the characteristic localized surface plasmon resonance (LSPR) bands observed in Au:Ag NPs, which describe the collective oscillation of the free surface electrons in quasi-spherical NPs induced by an electromagnetic wave in the UV-Vis range.^{36–39} A linear increase in the position of the LSPR band (λ_{max}) with the increment of the Au molar ratio indicates the formation of an Au:Ag nanoalloy rather than a core-shell growth, as shown in [Figure 1B](#).⁴⁰ Moreover, these results encompass 10 independent samples of each atomic composition, having standard deviations of ± 3 nm per NP type, indicating a high level of reproducibility of the synthesis method.³⁴ Additionally, [Supplementary Table S1](#) shows

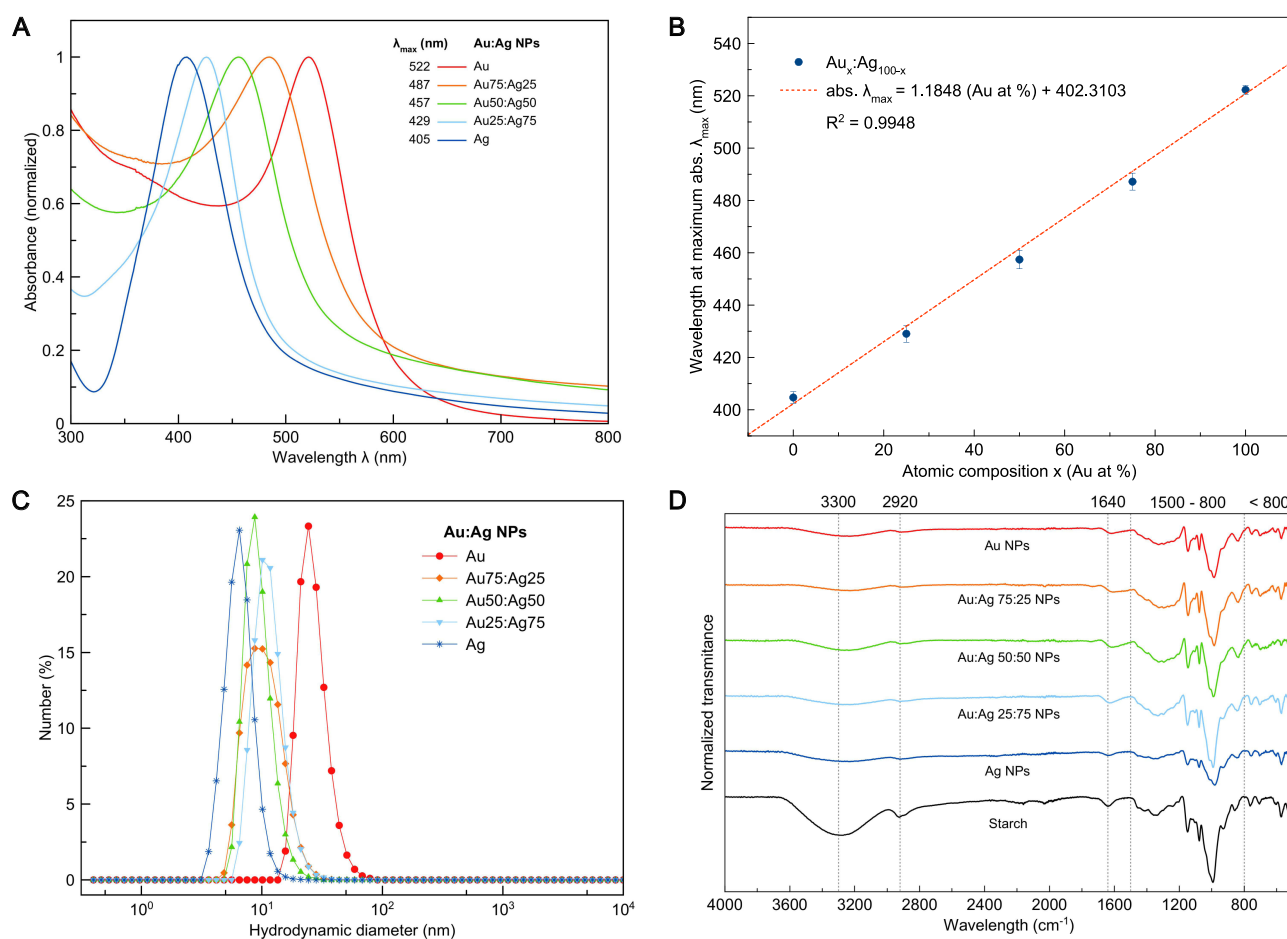


Figure 1 Physicochemical characterization of Au:Ag NPs. **(A)** Representative UV-vis absorption spectra. **(B)** Relation of the position of the LSPR band (λ_{\max}) and atomic composition of the NPs. The graph was constructed using 10 independent samples for each NPs system. **(C)** representative hydrodynamic diameter distribution obtained by DLS. **(D)** FT-IR spectra of the Au:Ag NPs compared with pure starch.

a comparison of λ_{\max} obtained in this work compared to the values reported in previous studies. In the cases of Au, Ag and Au50:Ag50 NPs the values are in close agreement. Stability studies were conducted to verify that the colloids did not lead to NPs agglomeration over time. The absorption spectra of the colloidal NPs were measured on the same day of their synthesis (day 0), on day 14, and again on day 26 after their synthesis to demonstrate the stability of the colloids ([Supplementary Figure S2A](#)). The results showed that the synthesis method yielded samples that showed colloidal stability for at least 26 days.

The XRD patterns for Au NPs, Ag NPs, and bimetallic Au:Ag NPs are shown in [Supplementary Figure S2B](#) along with the calculated XRD patterns for bulk face-centered cubic (FCC) Au and Ag.³⁵ The observed diffraction peaks at around $2\theta = 38.2^\circ$, 44.4° , 64.6° , 77.6° , and 81.8° for all the Au:Ag samples correspond to the crystallographic planes (111), (200), (220), (311), and (222), respectively, of Ag or Au with an FCC crystal structure.⁴¹ By analyzing the diffraction peaks associated with the (111) plane, it is possible to determine the cubic lattice parameter (a) of the FCC structure and the average crystallite size (L). The results obtained are presented in [Supplementary Table S2](#). It is noteworthy that the results fall within the expected range, with values close to 4.07 \AA ³³ and average values of the crystallite size (L) are relatively close to the corresponding average particle size found in DLS and TEM measurements (vide infra).

DLS is a widely employed technique to determine the hydrodynamic diameter of NPs in colloidal suspensions.⁴² As shown in [Figure 1C](#), the number-based measurements exhibited single peaks for the NPs, with D_H around 10 nm, excepting Au NPs, for which D_H was ~ 20 nm. The ζ -potential measurements were performed using the principles of ELS

Table 2 Hydrodynamic Diameter (D_H) and ζ -Potential of the Au:Ag NPs as Determined by DLS and ELS Measurements, Respectively

| NPs (Au:Ag) | D_H (nm) | ζ -potential (mV) |
|-------------|----------------|-------------------------|
| Au | 24.3 \pm 0.1 | -43.7 \pm 1.12 |
| Au75:Ag25 | 9.4 \pm 3.3 | -32.37 \pm 2.49 |
| Au50:Ag50 | 8.7 \pm 0.6 | -28.43 \pm 0.87 |
| Au25:Ag75 | 10.9 \pm 2.0 | -24.1 \pm 1.47 |
| Ag | 6.5 \pm 1.1 | -22.5 \pm 0.1 |

Abbreviations: NPs, Nanoparticles; Au:Ag, Gold:Silver; D_H , Hydrodynamic diameter.

to determine electrostatic repulsion between particles, thus influencing their stability in suspension. Generally, a colloid is considered stable if the ζ -potential is above a critical value of ± 30 mV.⁴³ Table 2 presents the obtained ζ -potential of Au, Ag, and Au:Ag NPs, whose values were around -30 mV, indicating that the colloids are near their critical threshold for stability. As the proportion of Ag increases, the absolute value of the ζ -potential decreases, suggesting that the addition of Au may improve the stability of the NPs.

The starch-coated NPs were investigated using FT-IR spectroscopy. The FT-IR spectra obtained from the Au, Ag and Au:Ag NP samples (Figure 1D) show the skeletal mode vibrations of the glucose pyranose ring, and markers of vibrations involving glycosidic linkage. Specifically, the stretching vibrations of the C-O-C glycosidic bridge can be observed between the ranges of 1160–1130 cm^{-1} and 999–965 cm^{-1} , while C-O-H bending and CH_2 twisting can be observed at 1344 cm^{-1} . The peak observed at 1640 cm^{-1} is characteristic of water adsorption in the amorphous regions of starch.^{44,45} These results are similar to the FT-IR spectrum of the powder starch used in the synthesis, thereby confirming the presence of a starch coating in the analyzed NPs.

Au:Ag NPs Showed Quasi-Spherical Morphology

The particle size and morphology of the synthesized Au, Ag, and Au:Ag NPs were investigated through TEM analysis. Figure 2 displays representative TEM images, which illustrate the quasi-spherical shape and uniformity of the synthesized NPs and their respective size distribution analysis. In the left insets of each type of NP in Figure 2, the particle size distribution is showed, presenting distributions of 22.68 \pm 1.7 nm, 13.30 \pm 3.6 nm, 12.43 \pm 4.1 nm, 12.35 \pm 4.3 nm, and 25.57 \pm 7.7 nm for Au NPs, Au75:Ag25, Au50:Ag50, Au25:Ag75 and Ag NPs, respectively.

Ag and Au:Ag NPs Reduce Mitochondrial Metabolism of Healthy and Hypertrophic H9c2 Cells

Previous reports demonstrated the cytotoxicity of Ag NPs on H9c2 cells,²² however, to the best of our knowledge, there are no reports regarding the cytotoxicity of noble metal-based NPs against cells under pathologic hypertrophic conditions, as well as on immune cells associated to metabolic disorders, such as MA macrophages. Therefore, here we evaluated the cytotoxic effect of Au NPs, Ag NPs and multiple bimetallic Au:Ag NPs alloys on hypertrophic H9c2 cells and MA macrophages. The hypertrophy on H9c2 cells were induced by Angiotensin-II as described in the methodology. The Angiotensin-II treated H9c2 cells showed more protein content per cell (Supplementary Figure S3) compared to untreated group, demonstrating that Angiotensin-II stimuli induced hypertrophy on H9c2 cells, in agreement with previous reports.^{46,47} In Figure 3, it can be observed the cytotoxic effect of Au:Ag NPs in different concentrations, from 0.1 to 10 ppm on macrophages (Figure 3A), MA macrophages (Figure 3B), H9c2 cells (Figure 3C) and hypertrophic H9c2 cells (Figure 3D) after 24 h of treatment. Our results exhibit that all NPs did not reduce more than 20% of the relative cell vitality on macrophages. Interestingly, on MA macrophages, all NPs between 1 and 5 ppm showed an apparent increase in cell vitality. On other hand, Ag NPs showed significant inhibition of the cell vitality in

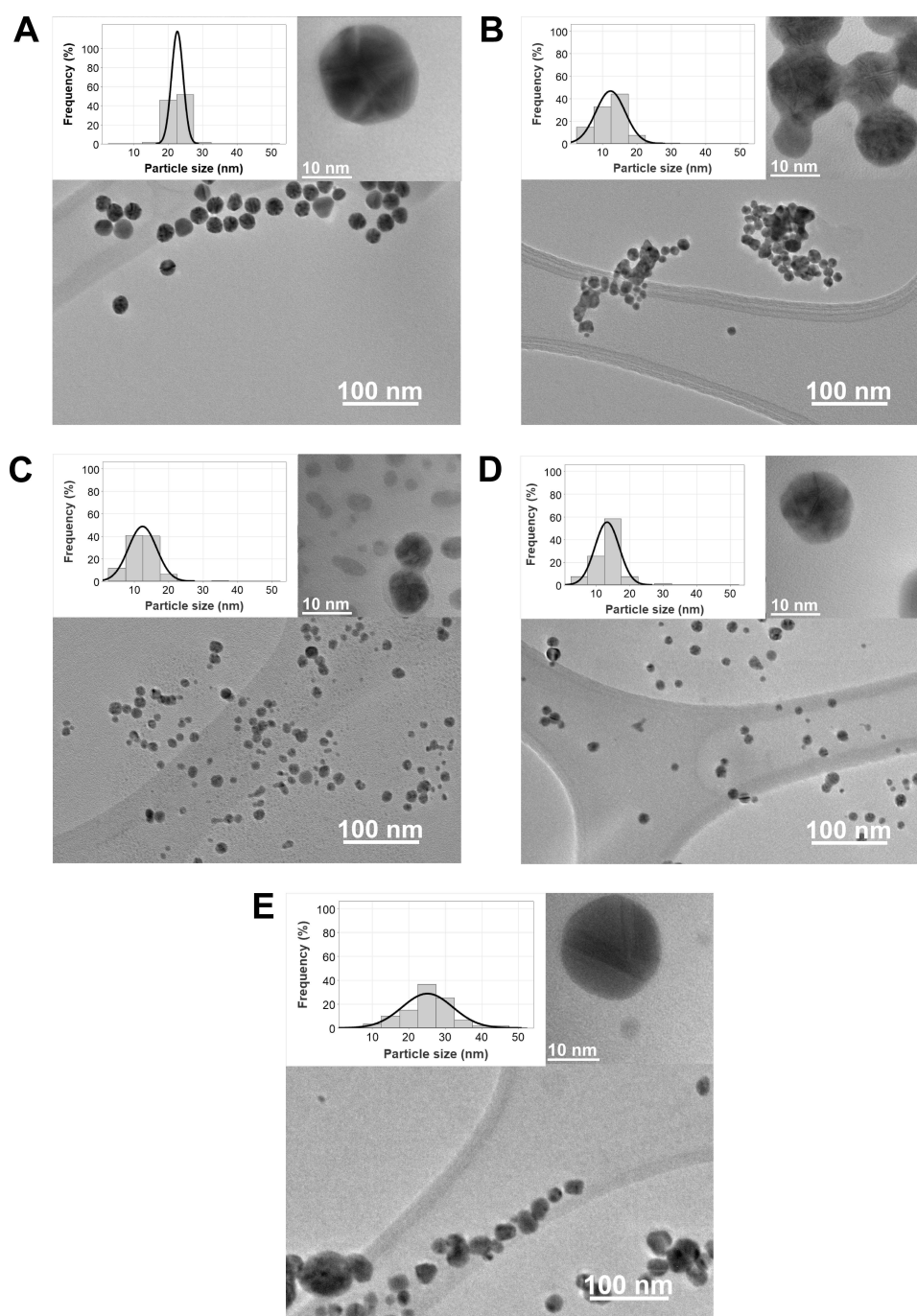


Figure 2 TEM analysis of mono- and bimetallic Au:Ag NPs. Representative electronic micrographs of: (A) Au, (B) Au75:Ag25, (C) Au50:Ag50, (D) Au25:Ag75, and (E) Ag NPs. For each NP, left insets show the particle size distribution histograms with a normal distribution fitting, and right insets show a representative particle magnification.

a concentration-dependent manner on H9c2 cells, contrary to Au NPs and the Au:Ag NPs alloys, where the cell vitality was not reduced more than 20%, ie, they were not cytotoxic. Table 3 shows the IC_{50} of Ag and Au25:Ag75 NPs on H9c2 cells, for which values of 7.06 ppm and >10 ppm, respectively, after 24 h were calculated. Another important finding was that on hypertrophic H9c2 cells the Ag NPs and Au25:Ag75 NPs decreased the relative cell vitality in a dose-dependent manner, while Au, Au75:Ag25 and Au50:Ag50 NPs did not significantly affect the relative cell vitality. The IC_{50} was 5.3 ppm and >10 ppm for Ag and Au25:Ag75 NPs after 24 h of stimuli (Table 3), respectively. These findings support the cytotoxicity of Ag NPs on H9c2 cells and highlight their higher cytotoxic effect against hypertrophic H9c2 cells,

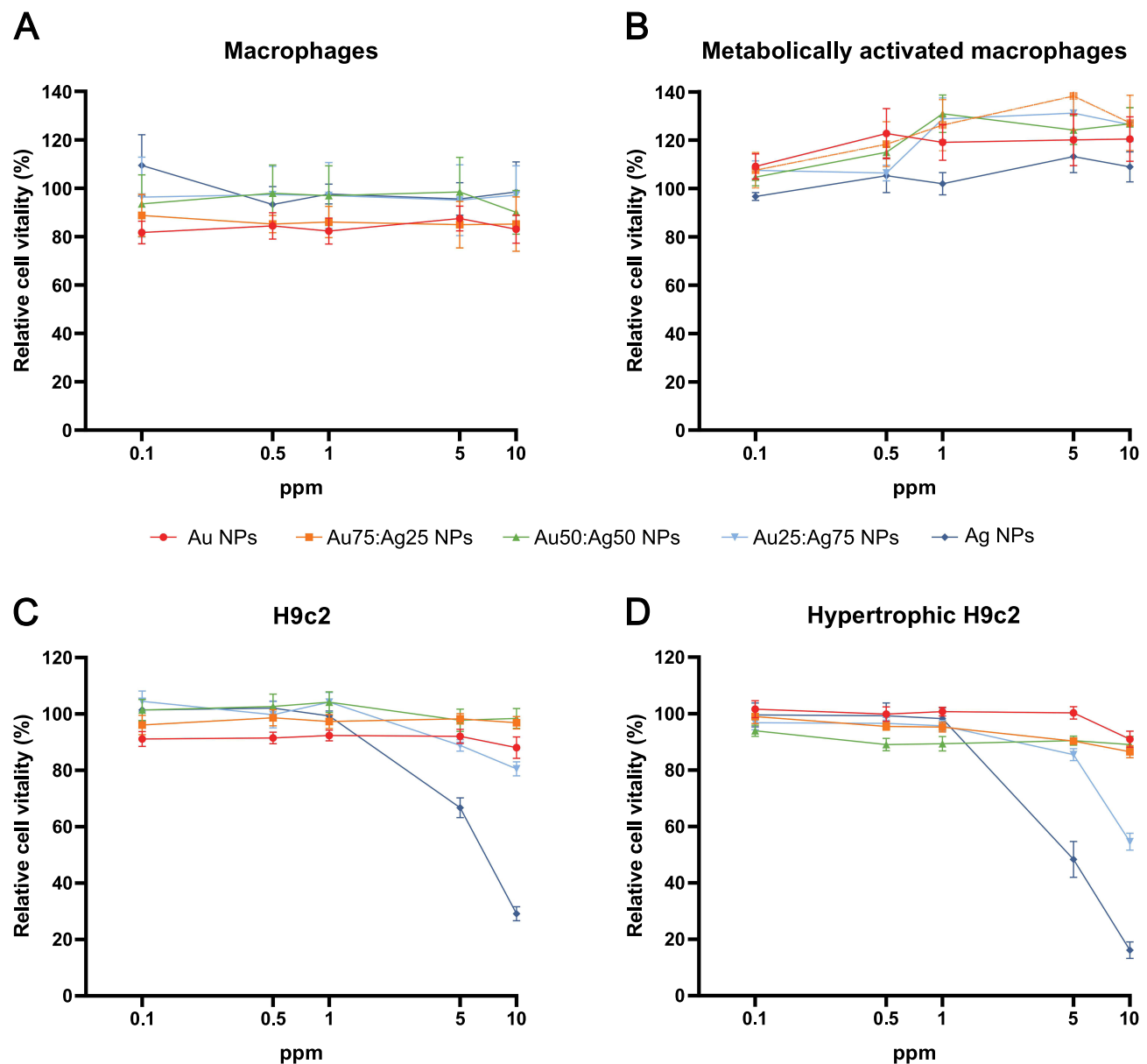


Figure 3 Cell vitality analysis on macrophages, metabolically activated (MA) macrophages, H9c2 and hypertrophic H9c2 cells. Relative cell vitality analysis quantification by Alamar blue assay on: (A) macrophages, (B) metabolically activated macrophages, (C) H9c2 and (D) hypertrophic H9c2 cells, treated at different concentrations with different concentrations (0.1, 0.5, 1, 5 and 10 ppm) of Au NPs, 75:25, 50:50, 25:75 and Ag NPs after 24 h. The percentages refer to relative cell vitality represented as percentage of control (non-treated cell vitality=100%). Data are presented as mean \pm SEM of triplicates of at least three independent experiments.

highlighting toxicological differences. Thus, we decided to elucidate the mechanism of cytotoxicity of the NPs on hypertrophic H9c2 cells based on the IC_{50} , here representing the threshold for 50% inhibition of the metabolic function of the cell culture.

To further visualize the mechanism of the NPs cytotoxicity, we first confirmed the cytotoxicity by analyzing the cytoplasmic esterase activity using ghost dye stain by flow cytometry at the IC_{50} of Ag and Au25:Ag75 NPs. Based on our previous cell vitality assay, where the IC_{50} Au25:Ag75 NPs was >10 ppm, we decided to estimate theoretically the IC_{50} value. In both H9c2 and hypertrophic H9c2 cells, the estimated IC_{50} was 12 ppm, which was the concentration employed for the following experiments. In Figure 4A it is observed that the percentage of viable H9c2 cells treated with Ag and Au25:Ag75 NPs was $87.57 \pm 8.6\%$, and $84.84 \pm 9.7\%$, respectively, whereas untreated cells showed $97.97 \pm 1.3\%$ of viable cells. Conversely, the percentage of viable hypertrophic H9c2 cells treated with the IC_{50} of Ag NPs and

Table 3 The Half of Inhibitory Concentrations (IC_{50}) for Ag and Au25:Ag75 NPs Indicated in ppm on H9c2 and Hypertrophic H9c2 Cells After 24 h of Stimuli

| NPs (Au:Ag) | H9c2 cells (ppm) | Hypertrophic H9c2 Cells (ppm) |
|-------------|------------------|-------------------------------|
| Au25:Ag75 | > 10 | ≥ 10 |
| Ag | 7.06 | 5.73 |

Abbreviations: NPs, Nanoparticles; Au25:Ag75, Gold 25%:Silver 75%; Ag, Silver.

Au25:Ag75 NPs was $55.22 \pm 13.2\%$, and $56.01 \pm 13.6\%$, respectively, while the untreated cells showed $95.89 \pm 1.6\%$. Representative dot plots are found in [supplementary Figure S4](#). These results confirm the high cytotoxicity of Ag and Au25:Ag75 NPs against hypertrophic H9c2 cells compared to non-hypertrophic (healthy) H9c2 cells.

Mitochondria is the major bioenergetic center of cells and the main reservoir of proteins involved in intrinsic apoptotic pathway. Mitochondrial alterations, such as loss of $\Delta\Psi_m$ or exacerbated mROS production, are associated with regulated cell death (RCD) or apoptosis.⁴⁸ To elucidate the mechanism of cytotoxicity of Ag and Au25:Ag75 NPs, we analyzed mitochondrial alterations on healthy and hypertrophic H9c2 cells. First, we evaluated the $\Delta\Psi_m$ using JC-1 stain by flow cytometry. The JC-1 stain allowed the differentiation of polarized mitochondria such as those high $\Delta\Psi_m$, versus depolarized mitochondria, such as those with low $\Delta\Psi_m$. Representative dot plots are found in [supplementary Figure S5](#). As shown in [Figure 4B](#), the control group showed $8.31 \pm 1.8\%$ of low $\Delta\Psi_m$, whereas treated cells with Ag and Au25:Ag75 NPs exhibit $50.13 \pm 24.5\%$ and $45.12 \pm 22.7\%$ of low $\Delta\Psi_m$, respectively. The positive control CCCP (80 nM) revealed $29.04 \pm 16.2\%$ of low $\Delta\Psi_m$. Similar trends were observed on hypertrophic H9c2 cells, ie, untreated cells showed $16.34 \pm 3.9\%$ of low $\Delta\Psi_m$, whereas $66.06 \pm 15.1\%$ and $68.92 \pm 16.3\%$ of low $\Delta\Psi_m$ were observed on Ag and Au25:Ag75 NPs-treated cells. CCCP treatment revealed $41.75 \pm 17.2\%$ of low $\Delta\Psi_m$. Thus, these results highlight that Ag and Au25:Ag75 produce loss of $\Delta\Psi_m$. Furthermore, we analyzed mROS production using MitoSox stain by flow cytometry. In [Figure 4C](#), we can observe representative histograms (left) and quantification (right) of the fold change of MitoSox MFI with respect to the control group on H9c2 cells, where the Ag NPs showed a 1.65 ± 0.8 fold increase, the Au25:Ag75 NPs revealed a 1.58 ± 0.6 fold increase, and the positive control H_2O_2 (50 μM) exhibited 1.81 ± 0.8 fold increase, all compared to the control group. On hypertrophic H9c2 cells, Ag NPs showed a 1.19 ± 0.1 fold increase, Au25:Ag75 NPs exhibited 1.28 ± 0.1 fold increase, and H_2O_2 (50 μM) exposed cells presented a 1.67 ± 0.3 fold increase, all compared to the control group. Overall, these data demonstrated that Ag and Au25:Ag75 NPs induce mitochondrial damage on healthy and hypertrophic H9c2 cells, suggesting an RCD.

Finally, to correlate the mitochondrial alterations induced by the Ag and Au25:Ag75 NPs with apoptosis, we analyzed phosphatidylserine exposure and membrane permeability by flow cytometry using Ann-V and PI stains, respectively. Positive cells for Ann-V, PI or both were considered as dead (RCD), and negative cells as live. In [Figure 4D](#), we can observe that the control group showed $7.12 \pm 2.7\%$, Ag NPs $37.60 \pm 5.5\%$, and Au25:Ag75 NPs $21.54 \pm 3.0\%$ of RCD. On hypertrophic H9c2 cells, control cells showed $8.08 \pm 2.3\%$, Ag NPs $29.17 \pm 2.5\%$, and Au25:Ag75 NPs $17.97 \pm 2.0\%$ of RCD. These results demonstrated that both metallic NPs induce RCD on healthy and hypertrophic H9c2 cells, albeit higher for Ag NPs.

Discussion

Nowadays, metallic NPs have gained significant attention for their wide biomedical applications due to their physico-chemical properties. Understanding the mechanisms underlying the cytotoxicity of metallic NPs upon metabolic disorders, such as cardiometabolic disease, is essential for mitigating potential risks and optimizing their use for biomedical applications. In this work, we analyzed the cytotoxicity of mono- and bimetallic Au:Ag NPs with different chemical compositions on healthy and hypertrophic H9c2 cells, and healthy and MA macrophages.

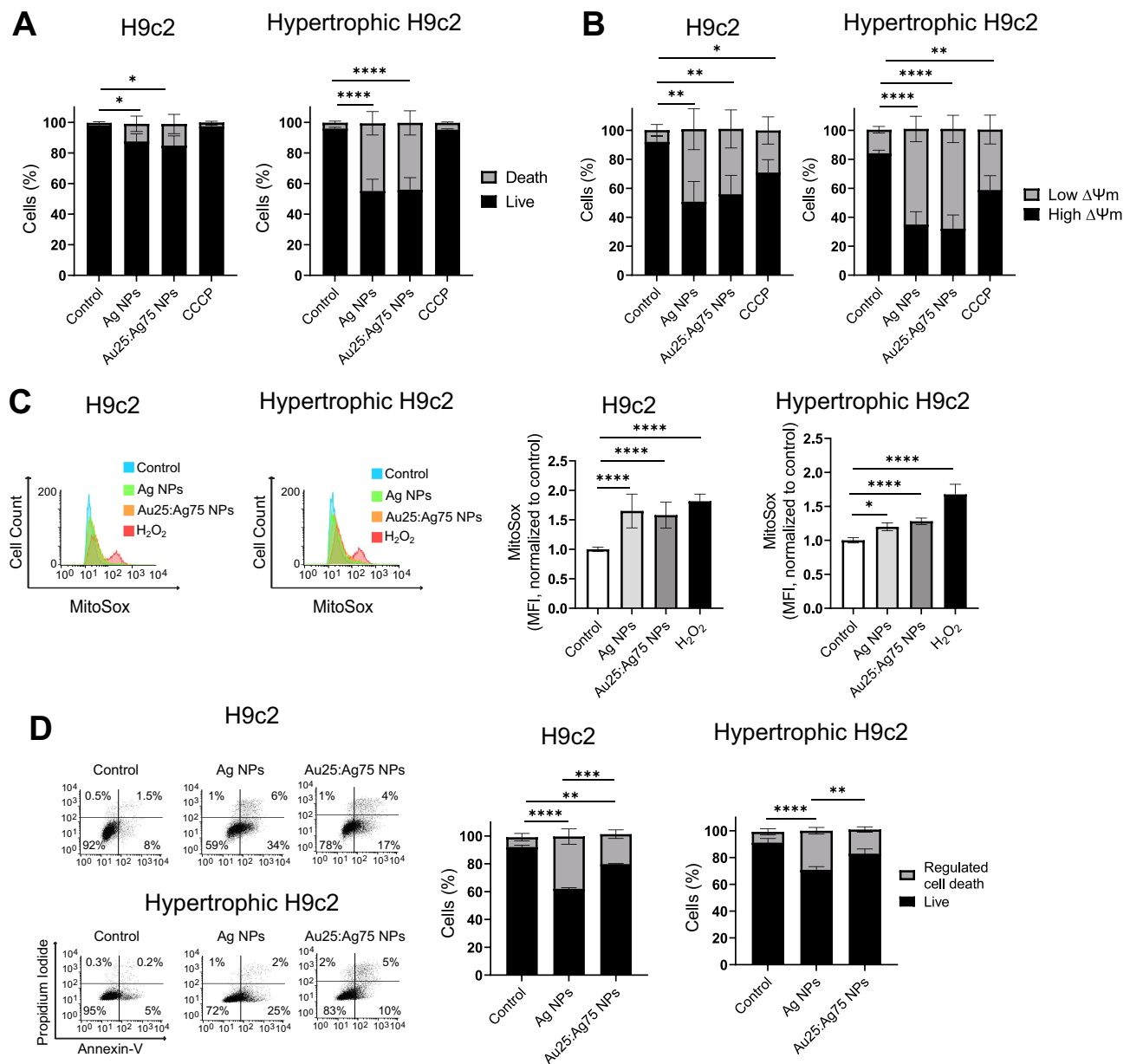


Figure 4 Biochemical implications of the cytotoxicity induced by Ag NPs and Au25:Ag75 NPs on healthy- and hypertrophic H9c2 cells. **(A)** Cell viability quantification using Ghost dye stain and, **(B)** mitochondrial membrane potential ($\Delta\Psi_m$) quantification using JC-1 stain by flow cytometry on H9c2 cells and hypertrophic H9c2 cells treated for 24 h with IC_{50} of Ag NPs and Au25:Ag75 NPs, and, CCCP (80 nM) as a positive control. **(C)** Mitochondrial reactive oxygen species (mROS) analysis and quantification using MitSox stain by flow cytometry on H9c2 cells and hypertrophic H9c2 cells treated with IC_{50} of Ag NPs, Au25:Ag75 NPs and H_2O_2 (50 μM) after 24 h of stimuli. **(D)** Regulated cell death analysis (left) and quantification (right) by flow cytometry using Annexin-V and PI stain on H9c2 cells and hypertrophic H9c2 cells treated with IC_{50} Ag NPs and Au25:Ag75 NPs at 24 h. Data are presented as mean \pm SEM of triplicates of at least three independent experiments. * $p < 0.05$, ** $p < 0.01$, *** $p < 0.001$, and **** $p < 0.0001$ compared to Control group (untreated cells).

Thus, we first determined the physicochemical properties of mono- and bimetallic NPs. In the case of the bimetallic Au:Ag NPs, the presence of single bands in the respective UV-Vis spectra is a strong indicator of the formation of nanoalloys (Figure 1A), and the absence of any additional signals or shoulders discard the presence of impurities or agglomerations.⁴⁹ Furthermore, the observed narrow bandwidth of the UV-Vis spectra indicates a low level of particle size polydispersity, suggesting a predominant proportion of NPs with similar particle sizes within a system.^{40,50} Furthermore, a linear monotonic increase of the position of the LSPR band (λ_{max}) with the atomic increment of Au indicates the formation of an Au:Ag nanoalloy rather than a core-shell growth.⁴⁰

As previously mentioned, the presence of starch in the NP samples was confirmed by FT-IR spectroscopy (Figure 1D), showing results consistent with those previously reported in the literature.^{33,34,36} Additionally, the stability studies previously described (Supplementary Figure S2A) demonstrate that starch effectively stabilizes the NPs in water for at least 26 days after their synthesis. The hydrodynamic diameter (D_H) distributions of the Au:Ag NPs systems lied within a range of 6–27 nm (Table 2). TEM images of Au75:Ag25 NPs showed a chain-like structure, similar to previous results reported by Nieto-Argüello et al.³⁴ However, its corresponding absorption spectrum shown in Figure 1A, displays only a single LSPR absorption band, ruling out the possibility of an anisotropic nanostructure. The mean diameter of the NPs (D_{mean}) as determined by TEM for Au and bimetallic Au:Ag NP systems are similar to the D_H and crystallite size (L) as determined by DLS and XRD, respectively. The increase in ζ -potential can be explained by the relatively poor stability of Ag due to its ease of ionization,⁵¹ as can be seen in Figure 2, where the monometallic Ag NPs and bimetallic Au:Ag NPs present agglomerations, unlike the Au NPs.

After characterizing the mono- and bimetallic Au:Ag NPs, we determined their cytotoxicity on healthy and MA macrophages, and healthy and hypertrophic H9c2 cells. In our results, we did not observe significant cytotoxicity in any macrophage (Figures 3A and 3B). These results are similar to previous studies which demonstrated the non-cytotoxic effect of Ag⁵² and Au NPs upon human peripheral mononuclear cells (primary culture of macrophages and lymphocytes),^{53,54} and on either pro- (M1) and anti- (M2) inflammatory macrophages, and Ag NPs modulated pro- and anti-inflammatory cytokines release.⁵⁵ Moreover, Ag NPs with smaller particle sizes (< 4 nm) induced more pro-inflammatory cytokines release on U937 cells than bigger Ag NPs (> 4 nm).⁵⁶ Our Au and Au:Ag NPs have smaller particle sizes than the Ag NPs; thus, the former NPs may promote pro-inflammatory cytokines release. This assumption could explain the slight cell vitality increase on MA macrophages induced by Au and Au:Ag NPs but not by Ag NPs.

On the other hand, Ag NPs showed significant cytotoxicity in a concentration-dependent manner on both healthy and hypertrophic H9c2 cells, but the Au NPs and bimetallic Au:Ag NPs do not show more than 20% cytotoxicity (Figure 3). Previously, the cytotoxicity of Ag NPs was demonstrated against H9c2 cells,²² whereas Au NPs with a mean particle size of 20 nm did not show cytotoxicity on the same cell line, contrary to Au NPs with particle sizes of 5, 40 and 100 nm that decreased cell vitality on H9c2 cells.⁵⁷ However, alloying Ag with platinum (Pt) increased the toxicity of NPs in vivo tests on zebrafish embryos.^{58,59} In other CVD contexts, Au NPs based on curcumin demonstrated cardio-protective effects in an in vivo model upon cardiac injury by a conventional chemotherapy (doxorubicin).⁶⁰ Thus, the reduction of the cytotoxic effect of the Ag NPs on healthy and hypertrophic H9c2 cells when alloying them with Au to form Au:Ag NPs could suggest a cardioprotective effect of the bimetallic nanomaterials.

Additionally, we demonstrated that Ag and Au25:Ag75 NPs induce mitochondrial alterations, specifically with regards the loss of $\Delta\Psi_m$, which is exacerbated on hypertrophic H9c2 cells and the mROS production that is attenuated on hypertrophic H9c2 cells (Figure 4C). This loss of $\Delta\Psi_m$ is likely due to excess of Ag ionization, increasing mROS, an effect similar to that produced by SiO₂ NPs,⁶¹ which under certain conditions could lead to cardiac fibrosis.⁶² This effect could be counteracted with antioxidants capable of reaching mitochondria such as quercetin in polymeric NPs⁶³ or mitochondrial antioxidant compounds.⁶¹ It is conceivable that mitochondrial damage could be attenuated by loading the metallic NPs with antioxidant molecules, even as a cardioprotective strategy.

Also, we revealed that the mechanism of cytotoxicity of Ag and Au25:Ag75 NPs induced the increase of mROS production and the loss of $\Delta\Psi_m$, associated to diminution of esterase activity and high RCD (Figure 4). Similarly, it has been previously demonstrated that Ag and Au NPs have shown to induce mitochondrial dysfunction such as ROS production, overexpression of pro-apoptotic proteins, loss of $\Delta\Psi_m$ and autophagy in variety of human, mouse and rat cells, including H9c2 cells.^{53,54,64,65} Such mitochondrial dysfunction is correlated with a dysregulation of Ca²⁺-ROS homeostasis⁶⁶ and thus, the demodulation of the mitochondrial Ca²⁺ dynamics, which are essential to bioenergetic balance and are likely a key player behind CVDs.^{46,67} Mitochondrial disruptions result in decreased cellular metabolism and bioenergetics activity, which accelerates cell death and autophagy.⁶⁸ Higher expression of genes associated with intrinsic apoptosis (p53, caspase-3 and Bax/Bcl-2) is correlated with high molar ratio of Ag in the Au:Ag alloy on human cancer cell lines (HCT116, 4T1 and HUH7).²⁵ Higher levels of ROS production were observed on Ag NPs compared to Au NPs and Au:Ag bimetallic NPs on the human breast cell line MCF-10A.⁶⁹

ROS are second messengers in a variety of signaling cascades⁷⁰ at low ROS levels, they have been shown to play a role in hypertrophy signaling, and at high levels induce cell death.⁷¹ Also, ROS accumulation directly contributes to Angiotensin II-induced hypertrophic cardiomyocyte by saturation and decrease of antioxidant enzymes activity.^{72,73} The fact that Ag NPs increase mROS production compared to Au₂₅:Ag₇₅ NPs on healthy and hypertrophic H9c2 cells suggests the possibility that Ag NPs induce higher levels of RCD, whereas the Au₂₅:Ag₇₅ NPs could ameliorate hypertrophy as remodeling to prevent cytotoxicity. The cardiac cells under pathologic hypertrophy condition revealed prominent susceptibility to reduce mitochondrial metabolism and function (Figure 4), leading to a slight increase in mROS production compared to healthy H9c2 cells. Regarding regulated cell death mechanism, both healthy and hypertrophic cardiac cells showed comparable results, showing a higher effect for Ag NPs than Au₂₅:Ag₇₅ NPs (Figure 4). The implication of alloying Ag with Au to create bimetallic Au:Ag NPs to attenuate their cytotoxicity encourages the potential application of such advantageous NPs in biomedical applications, including obesity-associated disorders. For example, the generation of safer and low-cost Au-based NPs for cardiac laser ablation in cardiac pathologies, or photo-thermal therapy on cancers, such as those of breast, liver, and pancreas.^{26,74,75} In general, there are many clinical applications of metallic NPs in the context of CVDs. For example, for imaging and detection Au:Ag NPs could be used as a contrast agent in imaging technologies.⁷⁶ Also, therapeutic agents as a drug delivery system that could be conjugated with cardiovascular drugs,⁷⁷ and anti-inflammatory applications, where Au NPs could act as an immunomodulator agent.^{78,79} But the first step towards an application is to identify the cytotoxicity of the noble metal-based NPs in pathological hypertrophy conditions. In this context, we have characterized bimetallic Au:Ag NPs with low nanotoxicity that may be employed for clinical application, such in the treatment of metabolic disorders.

Conclusion

Overall, our results demonstrate for the first time the cytotoxicity of the Ag and alloyed bimetallic Au₂₅:Ag₇₅ NPs against MA macrophages and cardiac cells under pathological hypertrophic conditions. Ag and Au₂₅:Ag₇₅ NPs induce regulated cell death, interestingly, with a major sensitivity on hypertrophic H9c2 cells, as evidenced by a marked reduction in metabolism and $\Delta\Psi_m$. This work helps to understand the potential cytotoxicity of mono- and bimetallic Au:Ag NPs on macrophages and cardiac cells under pathological conditions, highlighting their potential biomedical uses of those NPs with low Au-content. Finally, this study is the first step to provide evidence that pathological conditions related to metabolic disorders, such as obesity-associated cardiometabolic diseases, may have a higher susceptibility to certain noble metal-based NPs.

Acknowledgments

The authors thank Fátima Miroslava Alvarado Monroy and Elda Gomez for technical help. M. R. M. thanks CONAHCyT for scholarship funding. Also, the authors thank Hospital Zambrano Hellion and the Department of Science at Tecnológico de Monterrey, campus Monterrey for the facilities provided to perform this work.

Author Contributions

All authors made a significant contribution to the work reported, whether that is in the conception, study design, execution, acquisition of data, analysis and interpretation, or in all these areas; took part in drafting, revising or critically reviewing the article; gave final approval of the version to be published; have agreed on the journal to which the article has been submitted; and agree to be accountable for all aspects of the work.

Funding

The authors thank the financial support from Tecnológico de Monterrey through the Challenge-Based Research Funding Program 2022 (Project ID IJXT070-22EG57001).

Disclosure

The authors declare no conflict of interest.

References

- Khan SU, Saeed S, Alsuhaibani AM, et al. Advances and challenges for GWAS analysis in cardiac diseases: a focus on Coronary Artery Disease (CAD). *Curr Probl Cardiol.* 2023;48(9):101821. doi:10.1016/j.cpcardiol.2023.101821
- Valenzuela PL, Carrera-Bastos P, Castillo-García A, Lieberman DE, Santos-Lozano A, Lucia A. Obesity and the risk of cardiometabolic diseases. *Nat Rev Cardiol.* 2023;20(7):475–494. doi:10.1038/s41569-023-00847-5
- Avelar E, Cloward TV, Walker JM, et al. Left ventricular hypertrophy in severe obesity: interactions among blood pressure, nocturnal hypoxemia, and body mass. *Hypertension.* 2007;49(1):34–39. doi:10.1161/01.HYP.0000251711.92482.14
- Flier JS. Obesity wars: molecular progress confronts an expanding epidemic. *Cell.* 2004;116(2):337–350. doi:10.1016/S0092-8674(03)01081-X
- Nollet EE, Daan Westenbrink B, de Boer RA, Kuster DWD, van der Velden J. Unraveling the genotype-phenotype relationship in hypertrophic cardiomyopathy: obesity-related cardiac defects as a major disease modifier. *J Am Heart Assoc.* 2020;9(22). doi:10.1161/JAHA.120.018641
- Lindstrom M, Decléene N, Dorsey H, et al. Global burden of cardiovascular diseases and risks collaboration, 1990–2021. *J Am Coll Cardiol.* 2022;80(25):2372–2425. doi:10.1016/j.jacc.2022.11.001
- Zaromytidou M, Savvatis K. The weight of obesity in hypertrophic cardiomyopathy. *Clin Med J R Coll Physicians Lond.* 2023;23(4):357–363. doi:10.7861/clinmed.2023-0194
- Jiang W, Rutherford D, Vuong T, Liu H. Nanomaterials for treating cardiovascular diseases: a review. *Bioact Mater.* 2017;2(4):185–198. doi:10.1016/j.bioactmat.2017.11.002
- Azharuddin M, Zhu H, Das D, et al. A repertoire of biomedical applications of noble metal nanoparticles. *Chem Commun.* 2019;55:6964–6996. doi:10.1039/x0xx00000x
- Mouton AJ, Li X, Hall ME, Hall JE. Obesity, hypertension, and cardiac dysfunction novel roles of immunometabolism in macrophage activation and inflammation. *Circ Res.* 2020;126(6):789–806. doi:10.1161/CIRCRESAHA.119.312321
- Iacobellis G. Epicardial adipose tissue in contemporary cardiology. *Nat Rev Cardiol.* 2022;19(9):593–606. doi:10.1038/s41569-022-00679-9
- Papotti B, Opstad TB, Åkra S, et al. Macrophage polarization markers in subcutaneous, pericardial, and epicardial adipose tissue are altered in patients with coronary heart disease. *Front Cardiovasc Med.* 2023;10:1–12. doi:10.3389/fcvm.2023.1055069
- Khan SU, Saeed S, Sheikh AN, et al. Crafting a blueprint for microRNA in cardiovascular diseases (CVDs). *Curr Probl Cardiol.* 2023;48(12). doi:10.1016/j.cpcardiol.2023.102010
- Wang AZ, Langer R, Farokhzad OC. Nanoparticle delivery of cancer drugs. *Annu Rev Med.* 2012;63:185–198. doi:10.1146/annurev-med-040210-162544
- Lozano O, Torres-Quintanilla A, García-Rivas G. Nanomedicine for the cardiac myocyte: where are we? *J Control Release.* 2018;271:149–165. doi:10.1016/j.jconrel.2017.12.018
- Bostan HB, Rezaee R, Valokala MG, et al. Cardiotoxicity of nano-particles. *Life Sci.* 2016;165:91–99. doi:10.1016/j.lfs.2016.09.017
- Hu Q, Fang Z, Ge J, Li H. Nanotechnology for cardiovascular diseases. *Innovation.* 2022;3(2):100214. doi:10.1016/j.xinn.2022.100214
- Hernández-Fontes P, Lozano O, García-Rivas G. Nanomaterials aimed toward the cardiac mitochondria: from therapeutics to nanosafety. In: de OMR editor. *Mitochondrial Dysfunction and Nanotherapeutics.* Academic Press; 2021:311–347. doi:10.1016/B978-0-323-85666-9.00002-4
- Lozano O, Solís-Castañol D, Cantú-Casas S, Mendoza Muraira PI, García-Rivas G. A review of quercetin delivery through nanovectors: cellular and mitochondrial effects on noncommunicable diseases. *Mol Nut Mitochondria.* 2023;363–382. doi:10.1016/c2020-0-02475-8
- Sabir F, Barani M, Mukhtar M, et al. Nanodiagnosis and nanotreatment of cardiovascular diseases: an overview. *Chemosensors.* 2021;9(4):67. doi:10.3390/chemosensors9040067
- Huerta-García E, Zepeda-Quiroz I, Sánchez-Barrera H, et al. Internalization of titanium dioxide nanoparticles is cytotoxic for H9c2 rat cardiomyoblasts. *Molecules.* 2018;23(8):1–15. doi:10.3390/molecules23081955
- Khan AA, Alanazi AM, Alsaif N, Al-anazi M, Sayed AYA, Bhat MA. Potential cytotoxicity of silver nanoparticles: stimulation of autophagy and mitochondrial dysfunction in cardiac cells. *Saudi J Biol Sci.* 2021;28(5):2762–2771. doi:10.1016/j.sjbs.2021.03.021
- Ramirez-Lee MA, Espinosa-Tanguma R, Mejía-Elizondo R, Medina-Hernández A, Martínez-Castañón GA, Gonzalez C. Effect of silver nanoparticles upon the myocardial and coronary vascular function in isolated and perfused diabetic rat hearts. *Nanomed Nanotechnol Biol Med.* 2017;13(8):2587–2596. doi:10.1016/j.nano.2017.07.007
- Katifelis H, Lyberopoulou A, Mukha I, et al. Ag/Au bimetallic nanoparticles induce apoptosis in human cancer cell lines via P53, CASPASE-3 and BAX/BCL-2 pathways. *Cells Nanomed Biotechnol.* 2018;46(sup3):S389–S398. doi:10.1080/21691401.2018.1495645
- Hedberg Y, Nordberg GF. Silver. *Handb toxicol met fifth ed.* 2022. 2:773–782. doi:10.1016/B978-0-12-822946-0.00026-X
- Aitio A, Nordberg M, Santonen T. *Gold and Gold Mining;* 2021. doi:10.1016/B978-0-12-822946-0.00013-1
- Saeed S, Ud Din SR, Khan SU, et al. Nanoparticle: a promising player in nanomedicine and its theranostic applications for the treatment of cardiovascular diseases. *Curr Probl Cardiol.* 2023;48(5):101599. doi:10.1016/j.cpcardiol.2023.101599
- Zhang Q, Iwakuma N, Sharma P, et al. Gold nanoparticles as a contrast agent for in vivo tumor imaging with photoacoustic tomography. *Nanotechnology.* 2009;20(39). doi:10.1088/0957-4484/20/39/395102
- Suliasih BA, Budi S, Katas H. Synthesis and application of gold nanoparticles as antioxidants. *Pharm.* 2024;71:1–19. doi:10.3897/PHARMACIA.71.E112322
- Li H, Xu H. Mechanisms of bacterial resistance to environmental silver and antimicrobial strategies for silver: a review. *Environ Res.* 2024;248:118313. doi:10.1016/j.envres.2024.118313
- Mallmann EJJ, Cunha FA, Castro BNMF, Maciel AM, Menezes EA, Fachine PBA. Antifungal activity of silver nanoparticles obtained by green synthesis. *Rev Inst Med Trop Sao Paulo.* 2015;57(2):165–167. doi:10.1590/S0036-46652015000200011
- Singh C, Mehata AK, Priya V, et al. Bimetallic Au–Ag nanoparticles: advanced nanotechnology for tackling antimicrobial resistance. *Molecules.* 2022;27(20):7059. doi:10.3390/molecules27207059
- Lomeli-Marroquín D, Medina-Cruz D, Nieto-Argüello A, et al. Starch-mediated synthesis of mono- and bimetallic silver/gold nanoparticles as antimicrobial and anticancer agents. *Int J Nanomed.* 2019;14:2171–2190. doi:10.2147/IJN.S192757
- Nieto-Argüello A, Medina-Cruz D, Pérez-Ramírez YS, et al. Composition-dependent cytotoxic and antibacterial activity of biopolymer-capped Ag/Au bimetallic nanoparticles against melanoma and multidrug-resistant pathogens. *Nanomaterials.* 2022;12(5):779. doi:10.3390/nano12050779

35. Bragg WH, Bragg WL. The reflection of X-rays by crystals. *Proc R Soc Lond Ser A-Contain Pap Math Phys Character.* 1913;88(605):428–438. doi:10.1098/rspa.1913.0040
36. Nieto-Argüello A, Torres-Castro A, Villaurrutia-Arenas R, et al. Green synthesis and characterization of gold-based anisotropic nanostructures using bimetallic nanoparticles as seeds. *Dalton Trans.* 2021;50(46):16923–16928. doi:10.1039/d1dt02804a
37. Boruah JS, Devi C, Hazarika U, et al. Green synthesis of gold nanoparticles using an antiepileptic plant extract: in vitro biological and photo-catalytic activities. *RSC Adv.* 2021;11(45):28029–28041. doi:10.1039/d1ra02669k
38. Brza MA, Aziz SB, Anuar H, et al. Green coordination chemistry as a novel approach to fabricate polymer:Cd(II)-complex composites: structural and optical properties. *Opt Mater.* 2021;116:111062. doi:10.1016/j.optmat.2021.111062
39. Ayinde WB, Gitari WM, Samie A. Optimization of microwave-assisted synthesis of silver nanoparticle by Citrus paradisi peel and its application against pathogenic water strain. *Green Chem Lett Rev.* 2019;12(3):225–234. doi:10.1080/17518253.2019.1627427
40. Mallin MP, Murphy CJ. Au-Ag_sub-10nm_Nano lett_2002.pdf. 2002
41. Suh IK, Ohta H, Waseda Y. High-temperature thermal expansion of six metallic elements measured by dilatation method and X-ray diffraction. *J Mater Sci.* 1988;23(2):757–760. doi:10.1007/BF01174717
42. Mourdikoudis S, Pallares RM, Thanh NTK. Characterization techniques for nanoparticles: comparison and complementarity upon studying nanoparticle properties. *Nanoscale.* 2018;10(27):12871–12934. doi:10.1039/c8nr02278j
43. Shnoudeh AJ, Hamad I, Abdo RW, et al. *Synthesis, Characterization, and Applications of Metal Nanoparticles.* Elsevier Inc.; 2019. doi:10.1016/B978-0-12-814427-5.00015-9
44. Kizil R, Irudayaraj J, Seetharaman K. Characterization of irradiated starches by using FT-Raman and FTIR spectroscopy. *J Agric Food Chem.* 2002;50(14):3912–3918. doi:10.1021/jf011652p
45. Wiercigroch E, Szafraniec E, Czamara K, et al. Raman and infrared spectroscopy of carbohydrates: a review. *Spectrochim Acta A Mol Biomol Spectrosc.* 2017;185:317–335. doi:10.1016/j.saa.2017.05.045
46. Alves-Figueiredo H, Silva-Platas C, Estrada M, et al. Mitochondrial Ca²⁺ uniporter-dependent energetic dysfunction drives hypertrophy in heart failure. *JACC Basic to Transl Sci.* 2024;9(4):496–518. doi:10.1016/j.jacbs.2024.01.007
47. Garcia-Rivas G, Lozano O, Bernal-Ramirez J, et al. Cannabidiol prevents heart failure dysfunction and remodeling through preservation of mitochondrial function and calcium handling. *JACC Basic to Transl Sci.* 2025.
48. Lee H, Sook Jhun B, Yoon Y. Role of mitochondrial morphology in bioenergetics. *Biophys J.* 2013;104(2):302a. doi:10.1016/j.bpj.2012.11.1681
49. Cholula-Diaz JL, Lomeli-Marroquín D, Pramanick B, Nieto-Argüello A, Cantú-Castillo LA, Hwang H. Synthesis of colloidal silver nanoparticle clusters and their application in ascorbic acid detection by SERS. *Colloids Surf B Biointerfaces.* 2018;163:329–335. doi:10.1016/j.colsurfb.2017.12.051
50. Ponarulselvam S, Panneerselvam C, Murugan K, Aarthi N, Kalimuthu K, Thangamani S. Synthesis of silver nanoparticles using leaves of Catharanthus roseus Linn. G. don and their antiplasmodial activities. *Asian Pac J Trop Biomed.* 2012;2(7):574–580. doi:10.1016/S2221-1691(12)60100-2
51. Mulenos MR, Lujan H, Pitts LR, Sayes CM. Silver nanoparticles agglomerate intracellularly depending on the stabilizing agent: implications for nanomedicine efficacy. *Nanomaterials.* 2020;10(10):1–15. doi:10.3390/nano10101953
52. Greulich C, Diendorf J, Gebmann J, et al. Cell type-specific responses of peripheral blood mononuclear cells to silver nanoparticles. *Acta Biomater.* 2011;7(9):3505–3514. doi:10.1016/j.actbio.2011.05.030
53. Lorenzo-Anota HY, Zarate-Triviño DG, Uribe-Echeverría JA, et al. Chitosan-coated gold nanoparticles induce low cytotoxicity and low ROS production in primary leucocytes, independent of their proliferative status. *Pharmaceutics.* 2021;13(7):942. doi:10.3390/pharmaceutics13070942
54. Martínez-Torres AC, Lorenzo-Anota HY, García-Juárez MG, Zarate-Triviño DG, et al. Chitosan gold nanoparticles induce different ROS-dependent cell death modalities in leukemic cells. *Int J Nanomed.* 2019;14:7173–7190. doi:10.2147/IJN.S221021
55. Lategan KL, Walters CR, Pool EJ. The effects of silver nanoparticles on RAW 264.7. Macrophages and human whole blood cell cultures. *Front Biosci.* 2019;24(2):347–365. doi:10.2741/4722
56. Park J, Lim DH, Lim HJ, et al. Size dependent macrophage responses and toxicological effects of Ag nanoparticles. *Chem Commun.* 2011;47(15):4382–4384. doi:10.1039/c1cc10357a
57. Zhang J, Ma A, Shang L. Effect of gold nanoparticles on H9C2 myoblasts and rat peripheral blood mononuclear cells. in *38th World Congress of the International Union of Physiological Sciences (IUPS) Rhythms of Life.* 2017:1–5.
58. Formaggio DMD, de Oliveira Neto XA, Rodrigues LDA, et al. In vivo toxicity and antimicrobial activity of AuPt bimetallic nanoparticles. *J Nanopart Res.* 2019;21(11). doi:10.1007/s11051-019-4683-2
59. Asharani PV, Lianwu Y, Gong Z, Valiyaveetil S. Comparison of the toxicity of silver, gold and platinum nanoparticles in developing zebrafish embryos. *Nanotoxicology.* 2011;5(1):43–54. doi:10.3109/17435390.2010.489207
60. Sharifiaghdam Z, Dalouchi F, Sharifiaghdam M, Shaabani E. Curcumin coated gold nanoparticles attenuates doxorubicin-induced cardiotoxicity via regulating apoptosis on mice model. *Clin Exp Pharmacol Physiol.* 2020;49:70–83. doi:10.22541/au.159741438.87275915
61. Lozano O, Silva-Platas C, Chapoy-Villanueva H, et al. Amorphous SiO₂ nanoparticles promote cardiac dysfunction via the opening of the mitochondrial permeability transition pore in rat heart and human cardiomyocytes. *Part Fibre Toxicol.* 2020;17(1):1–16. doi:10.1186/s12989-020-00346-2
62. Rossi S, Savi M, Mazzola M, et al. Subchronic exposure to titanium dioxide nanoparticles modifies cardiac structure and performance in spontaneously hypertensive rats. *Part Fibre Toxicol.* 2019;16(1):1–18. doi:10.1186/s12989-019-0311-7
63. Lozano O, Lázaro-Alfaro A, Silva-Platas C, et al. Nanoencapsulated quercetin improves cardioprotection during hypoxia-reoxygenation injury through preservation of mitochondrial function. *Oxid Med Cell Longev.* 2019;2019:1–14. doi:10.1155/2019/7683051
64. Dey S, Fageria L, Sharma A, et al. Silver nanoparticle-induced alteration of mitochondrial and ER homeostasis affects human breast cancer cell fate. *Toxicol. Rep.* 2022;9:1977–1984. doi:10.1016/j.toxrep.2022.10.017
65. Li J, Zhang B, Chang X, et al. Silver nanoparticles modulate mitochondrial dynamics and biogenesis in HepG2 cells. *Environ Pollut.* 2020;256:113430. doi:10.1016/j.envpol.2019.113430
66. Yan Y, Wei CL, Zhang WR, Cheng HP, Liu J. Cross-talk between calcium and reactive oxygen species signaling. *Acta Pharmacol Sin.* 2006;27(7):821–826. doi:10.1111/j.1745-7254.2006.00390.x

67. Lozano O, Marcos P, Lázaro-Alfaro AF, Sobrevia L, García-Rivas G, García-Rivas G. Targeting the mitochondrial Ca²⁺ uniporter complex in cardiovascular disease. *Acta Physiol.* 2023;237(4):1–25. doi:10.1111/apha.13946
68. Lee J, Giordano S, Zhang J. Autophagy, mitochondria and oxidative stress: cross-talk and redox signalling. *Biochem J.* 2012;441(2):523–540. doi:10.1042/BJ20111451
69. Li JL, Tian B, Li T, et al. Biosynthesis of Au, Ag and Au–Ag bimetallic nanoparticles using protein extracts of deinococcus radiodurans and evaluation of their cytotoxicity. *Int J Nanomed.* 2018;13:1411–1424. doi:10.2147/IJN.S149079
70. Sauer H, Wartenberg M, Hescheler J. Reactive oxygen species as intracellular messengers during cell growth and differentiation. *Cell Physiol Biochem.* 2001;11(4):173–186. doi:10.1159/000047804
71. Oyama K, Takahashi K, Sakurai K. Cardiomyocyte H9c2 cells exhibit differential sensitivity to intracellular reactive oxygen species generation with regard to their hypertrophic vs death responses to exogenously added hydrogen peroxide. *J Clin Biochem Nutr.* 2009;45(3):361–369. doi:10.3164/jcbn.09-47
72. Singh MV, Cicha MZ, Nunez S, Meyerholz DK, Chapleau MW, Abboud FM. Angiotensin II-induced hypertension and cardiac hypertrophy are differentially mediated by TLR3- and TLR4-dependent pathways. *Am J Physiol Heart Circ Physiol.* 2019;316(5):H1027–H1038. doi:10.1152/ajpheart.00697.2018
73. Brasier AR, Recinos A, Elelrisi MS, Runge MS. Vascular inflammation and the renin-angiotensin system. *Arterioscler Thromb Vasc Biol.* 2002;22(8):1257–1266. doi:10.1161/01.ATV.0000021412.56621.A2
74. Liu X, Zhou W, Wang T, et al. Highly localized, efficient, and rapid photothermal therapy using gold nanobipyramids for liver cancer cells triggered by femtosecond laser. *Sci Rep.* 2023;13(1):1–14. doi:10.1038/s41598-023-30526-x
75. Jain A, Bhattacharya S. Recent advances in nanomedicine preparative methods and their therapeutic potential for colorectal cancer: a critical review. *Front Oncol.* 2023;13:1–27. doi:10.3389/fonc.2023.1211603
76. Younis NK, Ghoubaire JA, Bassil EP, Tantawi HN, Eid AH. Metal-based nanoparticles: promising tools for the management of cardiovascular diseases. *Nanomed Nanotechnol Biol Med.* 2021;36:102433. doi:10.1016/j.nano.2021.102433
77. Tang C, Zhou K, Wu D, Zhu H. Nanoparticles as a novel platform for cardiovascular disease diagnosis and therapy. *Int J Nanomed.* 2024;19:8831–8846. doi:10.2147/IJN.S474888
78. MacRitchie N, Di Francesco V, Ferreira MFMM, Guzik TJ, Decuzzi P, Maffia P. Nanoparticle theranostics in cardiovascular inflammation. *Semin Immunol.* 2021;56:101536. doi:10.1016/j.smim.2021.101536
79. Fujita T, Zysman M, Elgrabli D, et al. Anti-inflammatory effect of gold nanoparticles supported on metal oxides. *Sci Rep.* 2021;11(1):1–10. doi:10.1038/s41598-021-02419-4

International Journal of Nanomedicine

Publish your work in this journal

The International Journal of Nanomedicine is an international, peer-reviewed journal focusing on the application of nanotechnology in diagnostics, therapeutics, and drug delivery systems throughout the biomedical field. This journal is indexed on PubMed Central, MedLine, CAS, SciSearch®, Current Contents®/Clinical Medicine, Journal Citation Reports/Science Edition, EMBase, Scopus and the Elsevier Bibliographic databases. The manuscript management system is completely online and includes a very quick and fair peer-review system, which is all easy to use. Visit <http://www.dovepress.com/testimonials.php> to read real quotes from published authors.

Submit your manuscript here: <https://www.dovepress.com/international-journal-of-nanomedicine-journal>

Dovepress
Taylor & Francis Group